Journal of Nuclear Materials 407 (2010) 143–150

Contents lists available at ScienceDirect

Journal of Nuclear Materials

journal homepage: www.elsevier.com/locate/jnucmat

Tensile fracture characteristics of nanostructured ferritic alloy 14YWT

Jeoung Han Kim [a,1], Thak Sang Byun [b,*], D.T. Hoelzer [b]

[a] Special Alloys Group, Korea Institute of Materials Science, Changwon, South Korea
[b] Materials Science and Technology Division, Oak Ridge National Laboratory, Oak Ridge, TN 37830, USA

ARTICLE INFO

Article history:
Received 11 June 2010
Accepted 29 September 2010

ABSTRACT

High temperature tensile fracture behavior has been characterized for the nanostructured ferritic alloy 14YWT (SM10 heat). Uniaxial tensile tests were performed at temperatures ranging from room temperature to 1000 °C in vacuum at a nominal strain rate of 10^{-3} s^{-1}. Comparing with the existing oxide dispersion strengthened (ODS) steels such as Eurofer 97 and PM2000, the nanostructured alloy showed much higher yield and tensile strength, but with lower elongation. Microstructural characterization for the tested specimens was focused on the details of fracture morphology and mechanism to provide a feedback for process improvement. Below 600 °C, the fracture surfaces exhibited a quasi-brittle behavior presented by a mixture of dimples and cleavage facets. At or above 600 °C, however, the fracture surfaces were fully covered with fine dimples. Above 700 °C dimple formation occurred by sliding and decohesion of grain boundaries. It was notable that numerous microcracks were observed on the side surface of broken specimens. Formation of these microcracks is believed to be the main origin of the poor ductility of 14YWT alloy. It is suggested that a grain boundary strengthening measure is essential to improve the fracture property of the alloy.

Published by Elsevier B.V.

1. Introduction

The ferritic alloys containing a high number density of nanoclusters have been considered as promising candidates for future fission and fusion reactors because of their superior high temperature mechanical properties and higher radiation resistance compared to other commercial materials [1–3]. Their superior properties originate from the presence of uniformly dispersed tiny Y_2TiO_5 or $Y_2Ti_2O_7$ particles or Y and Ti enriched nanoclusters which act as strong barriers for dislocation movement as well as sinks for trapping of radiation-generated helium atoms and point defects [4–7]. Further, the remarkable thermal stability of nanoclusters provides excellent high temperature strength and creep resistance up to 800 °C [8,9]. However, such improvement in mechanical strength is usually achieved at the expense of ductility and fracture toughness [9–11]. For example, the 12YWT alloy (nominal composition: Fe–12 wt.%Cr–3%W–0.4%Ti–0.25%Y_2O_3) revealed poor tensile ductility and fracture toughness with a ductile–brittle transition temperature (DBTT) around 100 °C [12].

A new alloy, designated 14YWT (nominal composition: Fe–14 wt.%Cr–3%W–0.4%Ti–0.25%Y_2O_3), has been developed as a further nanostructured material. This new alloy has 2 wt.% more Cr and 0.05 wt.% more Y_2O_3 than 12YWT, while the extrusion temperature was decreased from 1150 °C for 12YWT to 850 °C for 14YWT [8]. Fracture toughness testing revealed that the 14YWT (SM6 heat) had far superior fracture toughness compared to its predecessor 12YWT, with 14YWT having a cryogenic DBTT around −150 °C and upper-shelf K_{JIc} values around 175 MPa$\sqrt{m}$ [13]. As for the tensile test results, the 14YWT exhibited a higher strength than the 12YWT while its total elongation slightly lower than that of the 12YWT. For applications to nuclear reactor core structures, ductility improvement is essential and it requires fundamental understating of the deformation and fracture mechanism of 14YWT. Particularly, a fracture surface examination to elucidate the origin of poor fracture property is inevitable.

In this work the room and high temperature tensile fracture behavior of 14YWT alloy was investigated to understand the details of tensile fracture procedure. Fracture surfaces were analyzed to elucidate the roles of boundaries, nanoclusters, and carbide or oxide particles in the tensile fracture. The temperature dependence of fracture surface, the variation and size of dimple structure in particular, was discussed in detail. Throughout the discussion it was attempted to draw a recommendation to improve the fracture properties of the alloy.

2. Experimental

The 14YWT alloy used in this study was part of the 1.2 kg SM10 heat produced by Hoelzer in 2009, which has been a base material for many studies in latest years. It was produced by mechanical alloying a mixture of pre-alloyed powder having a nominal composition of Fe–14Cr–3W–0.4Ti (wt.%) and particle size ranging from

* Corresponding author. Tel.: +1 865 576 7738.
E-mail address: byunts@ornl.gov (T.S. Byun).
[1] Visiting Scientist at Oak Ridge National Laboratory.

0022-3115/$ - see front matter Published by Elsevier B.V.
doi:10.1016/j.jnucmat.2010.09.054

45 to 150 μm and 0.3% Y_2O_3 having a particle size ranging from 17 to 31 nm. The pre-alloyed Fe alloy powder was produced by Ar gas atomization by Special Metals Powder Division. The powder mixture was ball milled in Zoz CMO1 attritor mil for 40 h in a static Ar environment. The mechanically alloyed powder was filled into a mild steel can which was evacuated to a vacuum of ~1 Pa at a temperature of 400 °C, sealed and hot extruded at 850 °C. Then, a multi-step hot rolling was followed for ~40% thickness reduction. More detailed description for processing can be found elsewhere [14].

A subsized dogbone-type plate specimen with a gage section of 7.62 mm × 1.52 mm × 0.76 mm, which is called the SS-3 type specimen [15], was used for the tensile testing. All specimens were machined to have their length direction aligning with the extrusion direction (L-orientation). Tensile tests at room temperature were carried out in a screw-driven machine equipped with a high temperature vacuum furnace at a nominal strain rate of about 10^{-3} s^{-1}. Test temperatures ranged from room temperature to 1000 °C, and vacuum level in the chamber was controlled to be about 10^{-4} Pa during elevated temperature testing. The crosshead movement was recorded during testing to use as the amount of specimen elongation and its plastic component was used to calculate the uniform and total elongations (in %).

The microstructure after heat-treatment was characterized by a transmission electron microscopy (TEM). Three millimetre diameter disk specimens were cut by wire electro-discharge machining and thinned to ~100 μm thickness and electro-polished in a Tenupol-3 using an electrolyte solution of 75% methanol and 25% nitric acid at about −27 °C. For each fractured tensile specimen, the fracture surface and side surface in the necked region were observed in a scanning electron microscope (SEM).

3. Results and discussion

3.1. Microstructure before deformation

Fig. 1 shows the TEM photograph of the 14YWT (SM10) alloy, which consists of very fine near-equiaxed grains with diameters in the range of 100–300 nm, specifically 136 ± 14% (95% confidence interval). Grain size is relatively homogeneous because the thermo–mechanical treatments after mechanical alloying process have prevented the nanograins from abnormal growth due to the formation of nanoclusters and small oxide particles at the grain boundaries. It is also observed that some grains are slightly elongated along the extrusion direction but their aspect ratios do not exceed 5:1.

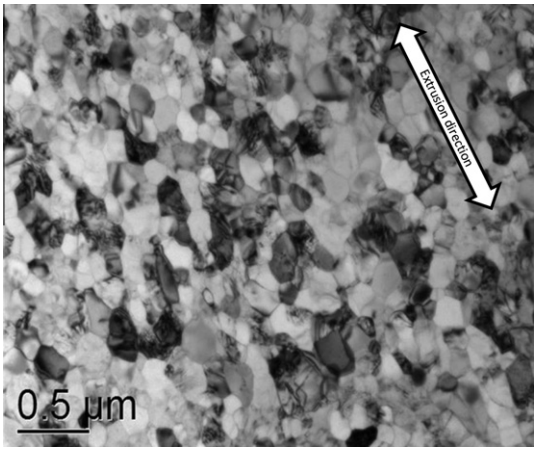

Fig. 1. TEM micrograph of the as-received 14YWT (10SM) specimen.

As seen in Fig. 2, the surface morphology of a non-deformed specimen observed in SEM also confirms the nanograin structure of the alloy. It is noted that there are relatively clear boundaries enclosing multiple grains, which are marked by white arrows in the picture and are discernable from the other less apparent boundaries. Each of these boundaries encloses an area with an effective diameter of about 10 μm or an aggregate of tens to hundreds of fine grains. The aggregates of grains are formed during ball

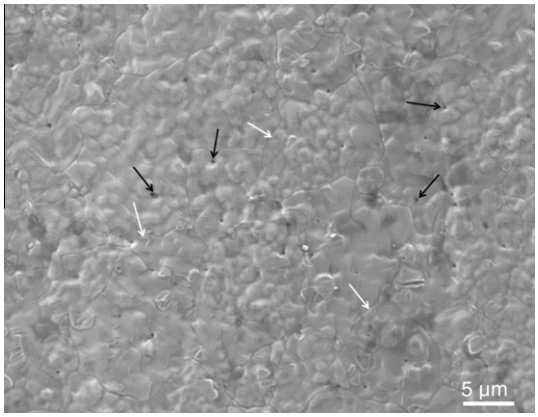

Fig. 2. SEM photograph showing the side surface of non-deformed tensile specimen (hot working direction: ↕).

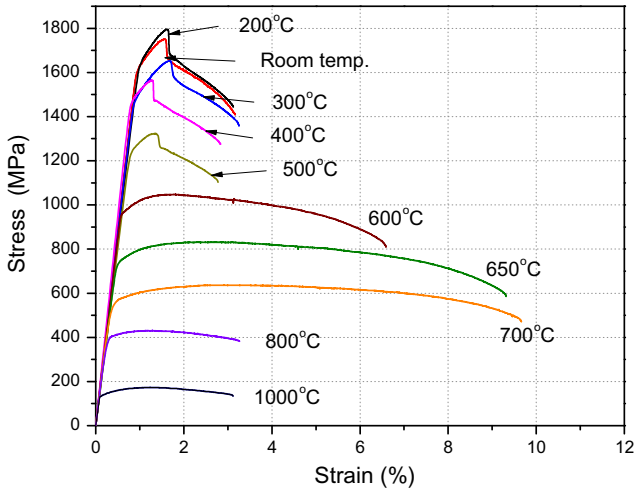

Fig. 3. Stress–strain curves of 14YWT at various temperatures for a nominal strain rate of 10^{-3} s^{-1}.

Table 1
Tensile data for 14YWT (10SM) alloy at various temperatures.

Temperature (°C)	YS (MPa)	UTS (MPa)	Total elongation (%)	Uniform elongation (%)	Reduction in area (%)
RT	1600	1749	2.4	0.7	31
200	1619	1792	2.4	0.7	25
300	1460	1651	2.5	0.8	–
400	1454	1558	2.2	0.5	–
500	1230	1322	2.2	0.7	19
550	1081	1181	3.0	0.9	–
600	952	1046	6.2	1.4	15
650	731	830	9.0	2.9	–
700	555	636	9.5	3.7	13
800	395	429	3.1	1.5	7
1000	133	172	3.1	1.5	7

milling process and come out as powders after the process. The surfaces of the aggregates are exposed to air before canning process and are believed to become the aggregate boundaries on compaction or extrusion process. It is speculated that these aggregate boundaries are decorated by thin oxidized layer; however, it could not be confirmed by EDAX data. As will be discussed later, these seem to have an important role in cracking process.

Another notable feature observed in the SEM picture is the existence of micropores, which might be formed from the entrapped inert gas used for mechanical alloying. In Fig. 2 some of the micropores are indicated by black arrows. The micropores seem to be randomly distributed over the whole specimen and some of them are located at the aggregate boundaries. These pores can be stress concentration points that can help generation and propagation of microcracks in fracture process.

3.2. Tensile curve behavior

Fig. 3 shows the engineering stress–strain curves obtained at temperatures ranging from room temperature to 1000 °C. Major engineering tensile properties are also summarized in Table 1. Between room temperature and 500 °C, the 14YWT alloy exhibits very high yield strength (YS; 0.2% offset yield strength) and ultimate tensile strength (UTS). For example, the YS and UTS at room temperature were 1600 MPa and 1749 MPa, respectively. These are considerably higher than those of the predecessor alloy 12YWT: 1300 MPa and 1400 MPa for YS and UTS, respectively [12]. The strength of 14YWT started to decrease with temperature from about 400 °C at relatively high rate and the rate of decrease appeared to be slowed above 800 °C. Although the decrease in the 400–800 °C region was significant, the 14YWT alloy still retained high YS and UTS of about 400 MPa. This is a remarkably high strength at such high temperature for steels.

Despite the 14YWT alloy displayed such high strengths over possible application temperature range (<800 °C), the measured total elongations were relatively low: 2.2–3.1% except for the temperature window of 600–700 °C, where it exhibited more than 6% total strain. A peak total elongation of 9.5% was obtained at 700 °C; however, the total elongation decreased back to ~3% above 800 °C. In the temperature range of room temperature −500 °C, the 14YWT alloy showed uniform strains of ⩽1% and significant load drops at the initiation of necking failure. This load drop disappeared and work hardening rate was low at or above 600 °C.

3.3. Temperature dependence of fracture surface after uniaxial tensile testing

Fig. 4 displays the fracture surface formed after significant localized necking at a room temperature (RT). In Fig. 4a, a low magnification picture, shows several large cracks propagated in the specimen length direction. These crevices in the perpendicular direction to the fracture surface are often accompanied by fracture protrusions and steps [16,17]. The formation of such large cracks is believed to be a reflection of hot working feature and existence of tensile stress component in the thickness direction during testing.

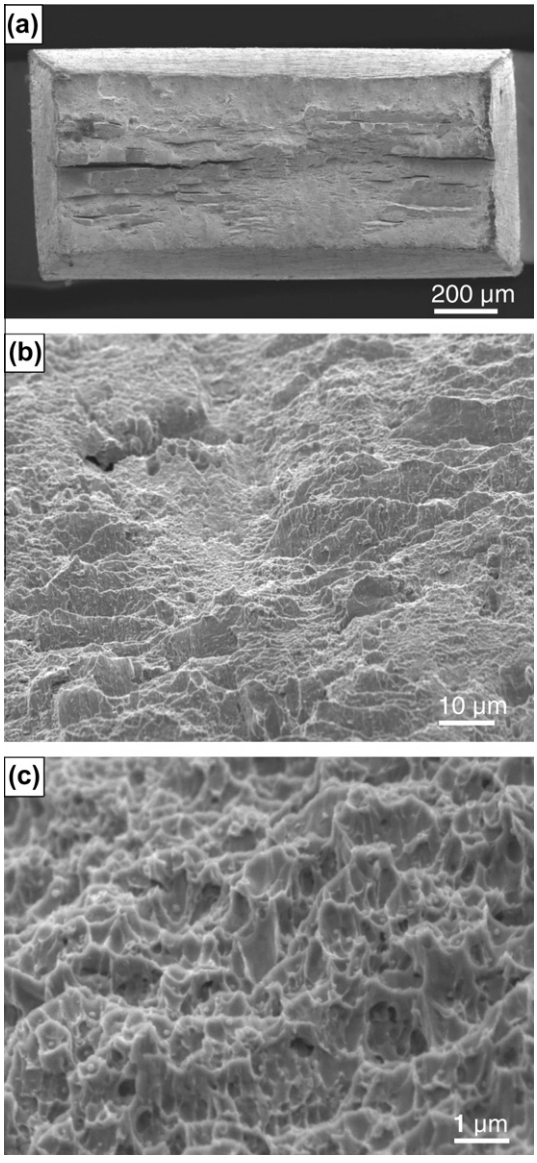

Fig. 4. Fractographs of 14YWT tension tested at room temperature: (a) a macro-view, (b) fracture surface showing cleavage planes, and (c) dimple structure containing small particles.

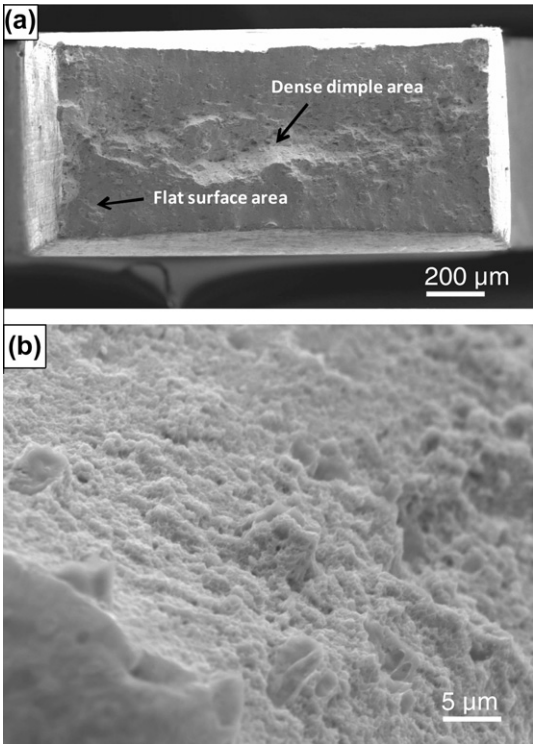

Fig. 5. Fractographs of 14YWT tension tested at 200 °C: (a) a macro-view and (b) dimple structure in centre area of specimen.

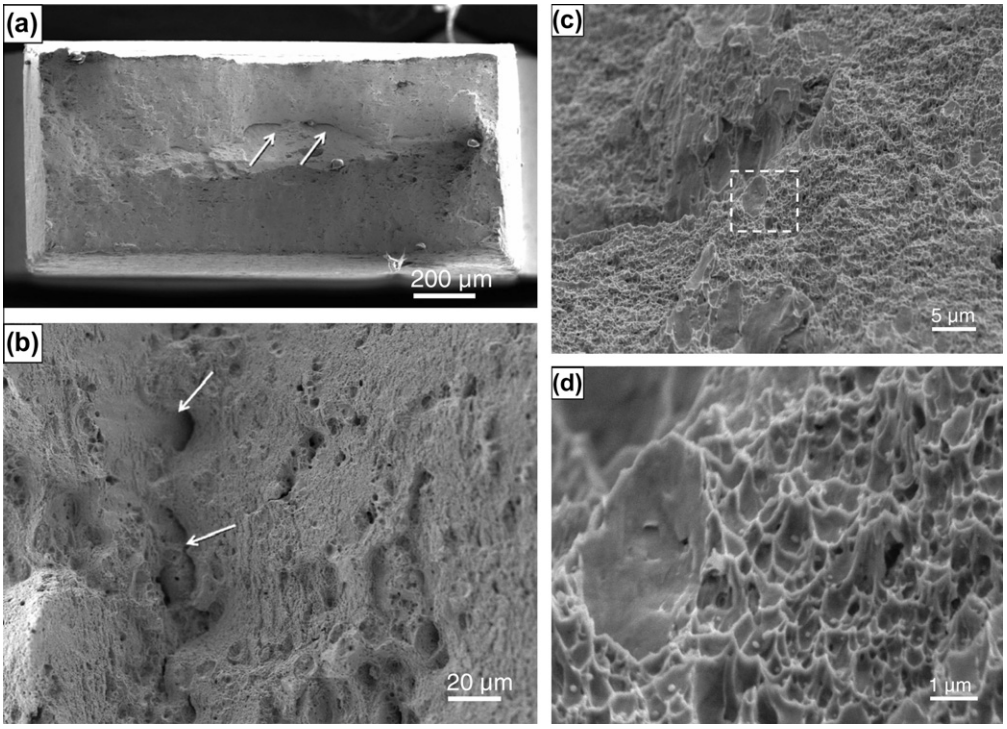

Fig. 6. Fractographs of 14YWT tension tested at 500 °C: (a) a macro-view, (b) magnified view of fracture surface parallel to loading axis, (c) fracture surface showing isolated facets in central area of specimen, and (d) zoomed-in image of the boxed area in (c).

A lamellar structure of slightly elongated grains was formed during the thermo-mechanical process consisting of preheating, hot extrusion and rolling, and the crevice type cracks seen in Fig. 4a formed along the lamellar boundaries.

More fracture mechanistic features are represented by a higher magnification picture: Fig. 4b is a fracture surface showing coarser cleavage facets and other finer structure area. This picture appears to be a typical fracture surface from semi-brittle fracture. In some area, if seen in higher magnification, fracture surface is full of fine dimples, Fig. 4c. It appears therefore that the fracture surface at room temperature consists of small cleavage facets linked by ductile ridges covered by dimples. This states that the tensile failure of 14YWT at room temperature is a quasi-brittle fracture.

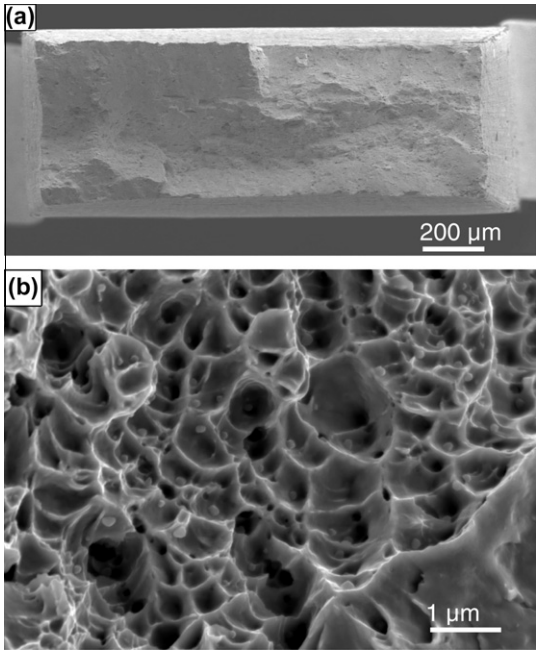

Fig. 7. Fractographs of 14YWT tension tested at 600 °C: (a) a macro-view and (b) magnified view showing dimple structure.

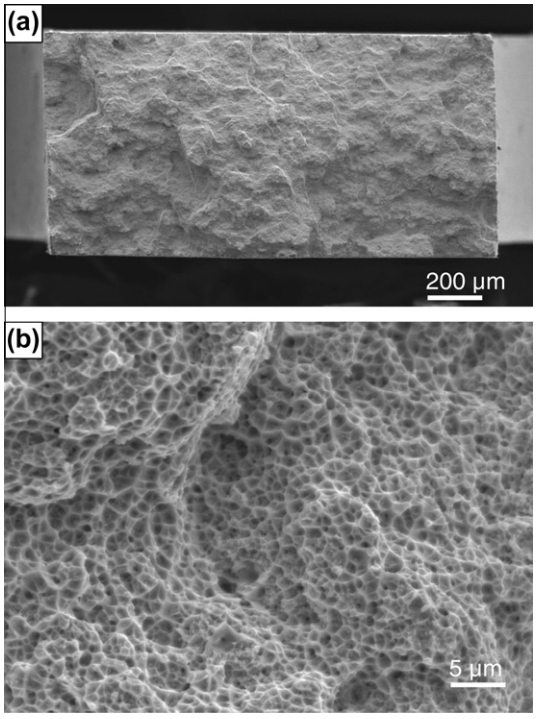

Fig. 8. Fractographs of 14YWT tension tested at 800 °C: (a) a macro-view showing little lateral contraction and (b) magnified view for dimple structure.

Also found in Fig. 4c are small spherical particles in many dimples. The diameter of the particles ranged from 100 nm to 200 nm and their volume fraction was measured to be 0.05–1%. In energy dispersive X-ray analysis, all the small precipitates are enriched in Ti and Cr (at a lower level) relative to the matrix. Some particles ~200 nm in size were enriched in Ti, Y, and Cr. It has been reported that such small particles were carbides particles [14]; however, the fact that the particle size of 100–200 nm is also the size of typical grains in 14YWT SM10 alloy can lead to a conclusion that these particles in dimples are nanograins. This indicates that the dimples are initiated by grain boundary decohesion. A further confirmation is needed.

Similar to the room temperature behavior, the specimen tested at 200 °C displays significant necking at failure but no large cracks, as shown in Fig. 5a. Fig. 5b is a fracture surface taken in the central area of the specimen, which has a dense array of round dimples. It has more ductile appearance than that of outer area which has flat surface. Fracture seems to begin at the central area and terminated at outer shear-lip zone. The size of dimples is small; some of them were below 200 nm in diameter and have probably been initiated on small carbide or oxide particles.

Fig. 6a–d are the fractographs of a 14YWT specimen broken at 500 °C. Comparing with the facture surfaces developed at lower temperatures, the number of cleavage-like surfaces is reduced significantly. Also, the cleavage-like surfaces seem to have been formed with some shear deformation. While the dimpled portion is dominant, some large cracks and shear planes are still observed (see arrows in Fig. 6a and b), which may be one of the reasons for low ductility at this temperature. At higher magnification, Fig. 6c, plenty of cleavage-like facets are observed even at this high temperature. Micropores were also found at in these fracture surfaces and are believed to be crack initiation and linking sites. The surface in Fig. 6d consists of numerous nanoscale dimples, some of which contain small particles.

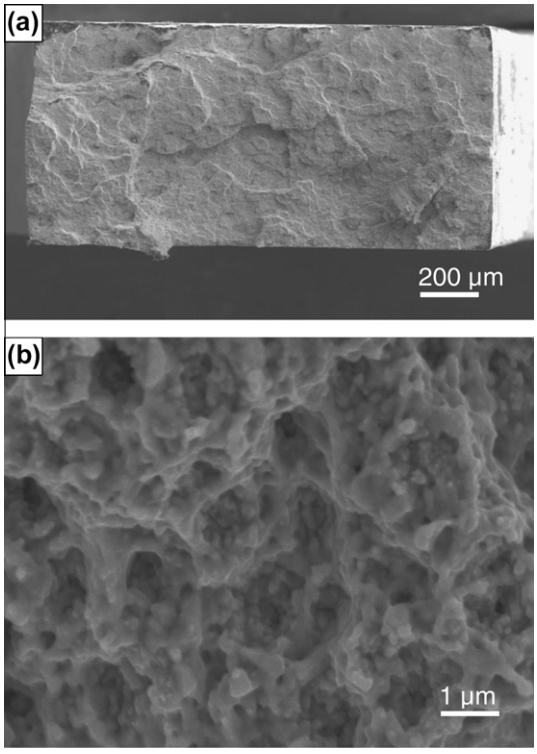

Fig. 9. Fractographs of 14YWT tension tested at 900 °C: (a) a macro-view showing little lateral contraction and (b) magnified view showing dimple structure.

At 600 °C, the tensile fracture mode changed to a fully-ductile fracture mode with formation of deeper dimples, Fig. 7a and b. Such change in fracture mode should be associated with relatively high tensile ductility at the temperature. In Fig. 7a large crevice type cracks are rarely seen and the surface looks like a non-glossy gray facets. Fig. 7b shows the dimple structure formed at 600 °C, which is similar to those formed at lower temperatures but the dimples are apparently deeper.

At 800 °C a typical failure feature consisted of ductile tearing and microvoid coalescence became dominant over the whole fracture surface. In Fig. 8, although dimpled structure is not discernable at low magnification, the fracture surface is fully covered with homogeneous dimple and no cleavage plane is found. Interestingly, dimple size increased significantly when compared to those formed at lower temperatures: from ~400 nm to ~750 nm. Also, it is noticed that the dimples have equiaxed shape with much distinctive boundaries.

Similar to the failure behavior at 800 °C, no localized necking was found and entire fracture surface is covered with dimples at

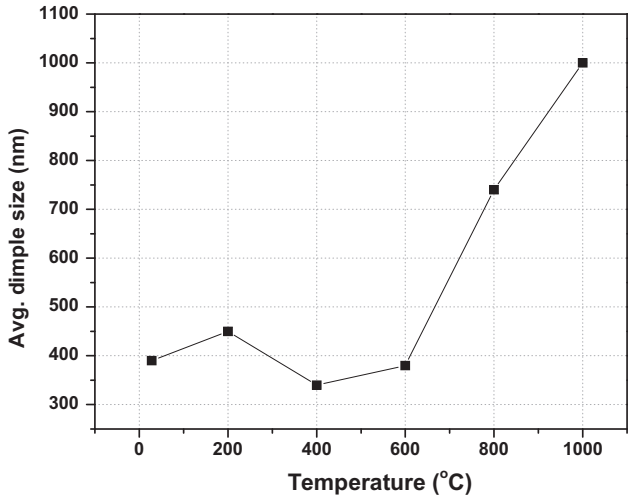

Fig. 10. Variation of dimple size as a function of temperature.

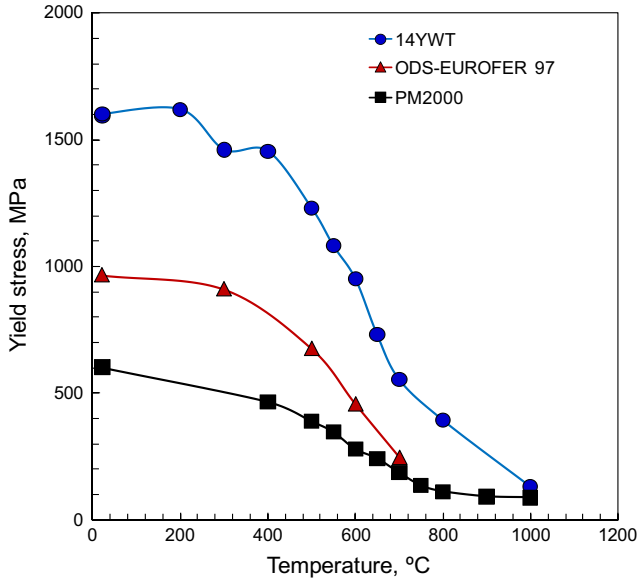

Fig. 11. Yield stress of 14YWT, ODS-EUROFER97, and PM2000 as a function of temperature [19].

900 °C, as seen in Fig. 9a and b. However, the dimple boundaries are not very distinctive and many small particles are found at the wall of dimples. These particles do not look like oxide or carbide particles, but they seem to be sub-microcrystalline grains which are separated from each other by boundary decohesion. It is believed that the highly viscoplastic boundaries at 900 °C have produced such a unique fracture surface showing both dimpled feature in micrometer scale and intergranular decohesion in smaller scale.

3.4. Dimple size variation with temperature

Fig. 10 presents the variation of dimple size with temperature. As mentioned above, the dimple size was below 400 nm until temperature increased up to 700 °C. A mechanism of void initiation at grain boundaries and subsequent coalescence following grain boundaries can explain the dimples slightly larger than grain sizes. Above this temperature, however, dimple size steeply increased with test temperature: the average dimple size was much larger than the grain diameters in the range 100–300 nm. The microstructure of 14YWT alloy was proven to have an excellent thermal stability [9,14]: the SM10 heat was annealed at 1000 °C for 1 h on two occasions during extrusion process but it still retained the nano-sized clusters and grains. Therefore, the grain growth is not considered as the reason for the larger-than-grain dimples. Presumably, there would be significant change in deformation mechanism around 700–800 °C.

At 900 °C, the dimple surfaces with numerous particles or grains should indicate that the dimples have been formed by a boundary decohesion process. A notable feature found in Fig. 9b is that the well-developed shear lips, which are common in ductile dimples, are not observed. This indicates that the amount of plasticity involved in the fracture process might be limited. Kumar et al. [18] explained similar behavior, which occurred in nanocrystalline nickel, by grain boundary sliding mechanism. In this 900 °C case, however, the average dimple size of ~1 μm is much larger

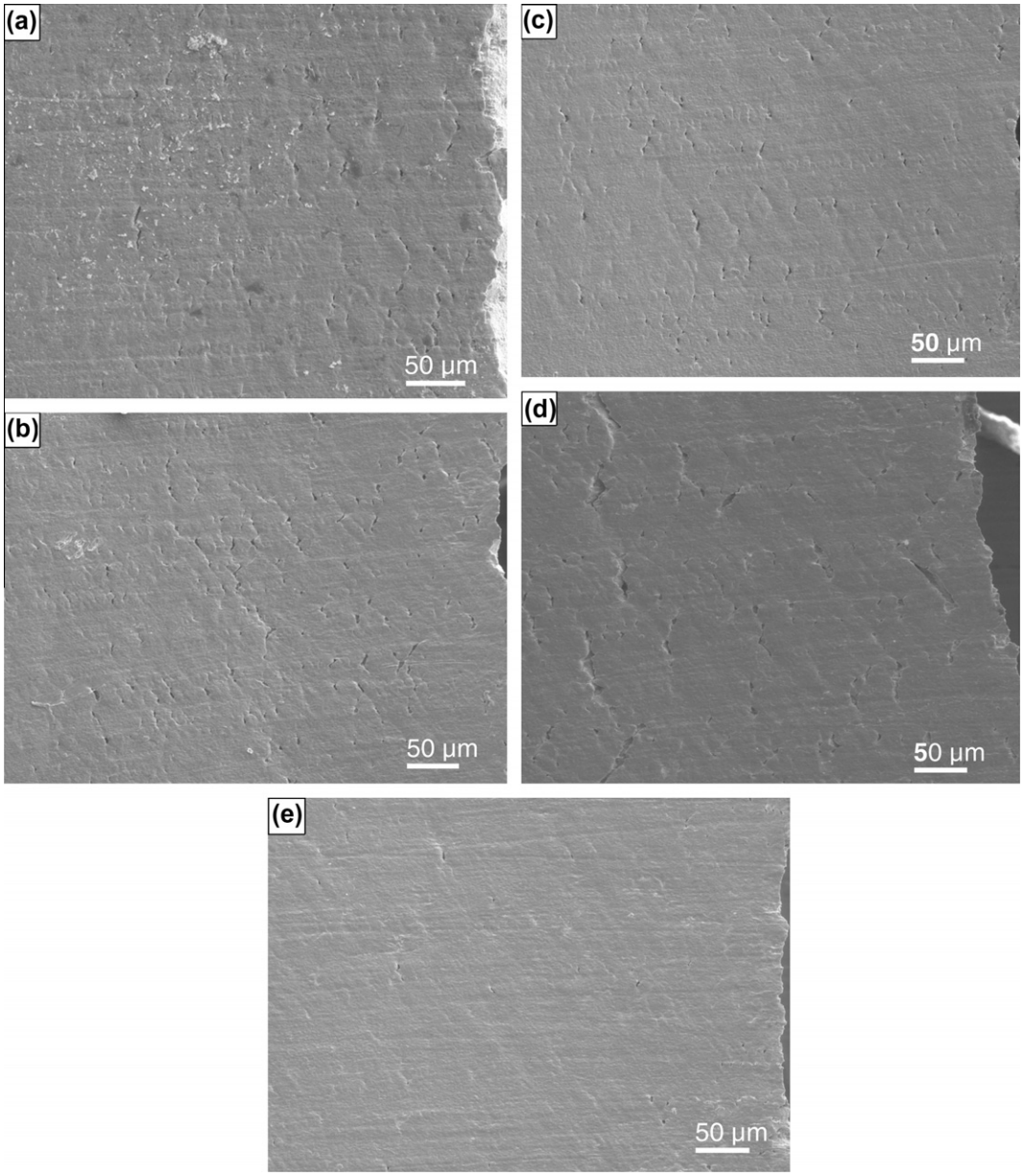

Fig. 12. Side surfaces of specimens broken at (a) room temperature, (b) 200 °C, (c) 500 °C, (d) 600 °C, and (e) 700 °C. (Loading axis and extrusion direction: ↔).

than the average grain size. This indicates that the cracking have proceeded along selected path of boundaries. It is believed therefore that the increased dimple size is caused by boundary separation after limited amount of sliding and plasticity occurring only at preferred boundaries enclosing multiple grains. Further, these preferred boundaries are believed to be the aggregate boundaries seen in Fig. 2.

3.5. Deformation and failure mechanism

Fig. 11 displays that the strength of 14YWT (SM10) alloy is much higher than other comparable alloys such as PM2000 and ODS-Eurofer 97 over the entire test temperature range [19]. Even compared to the earlier heats of the 14YWT alloy [12,14], the current version is significantly stronger due to its highly refined microstructure. However, such a high strength was achieved at the expense of ductility: the total elongations measured were as low as 2.2% at low temperatures (<500 °C) while those of ODS-Eurofer 97 and 12YWT alloy which are above ~10%. Since such a low ductility should result in low fracture toughness, an investigation on the poor ductility and fracture mechanism is essential. In the fractography results (Figs. 4–6) obtained for the temperatures ⩽500 °C, a mixture of numerous nanoscale dimples and cleavage planes were found at high magnification views. This can indicate that fracture has occurred in a mixed mode. An explanation for the cleavage formation would be a transgranular quasi-cleavage failure initiated from the aggregate boundaries (the clear boundaries in Fig. 2) due to their weak bonding. The remaining areas should develop to the ductile dimple-populated surfaces. It may be a surprise, however, that the total elongations measured were merely 3% or so, despite the presence of large dimpled areas. For example, at 500 °C where the population of cleavage planes was reduced significantly, the total elongation was only 2.2%. Further, the low ductility feature persisted above the narrow temperature window of 600–700 °C where rather higher total elongations (>6%) were measured and the fracture surfaces started to be entirely covered by larger dimples. It is obvious, therefore, that neither of the fraction of dimpled area nor the size of ductile dimples is well correlated to ductility.

In tensile tested specimens, the cracking process before final fracture can be deduced from the morphology of the side surfaces of necks. Since the specimens are relatively thin (0.762 mm), the axial stress component is the maximum principal stress through the specimen thickness and the surface fracture phenomenon is believed to represent the general failure mechanism in the necked region. Fig. 12a–e display numerous microcracks formed near the fracture surfaces at 200–700 °C. These microcracks were distributed on the surface up to ~500 μm from the fracture surfaces (or the right ends of the pictures). It is unusual for ductile material to have such a large number of microcracks in the fracture. Considering their population and size, it was easily concluded that the formation of these microcracks contributed to inelastic strain and were a major cause for the low tensile elongation. The inelastic strain component from such microcracking process can be a pseudo-ductility that can contribute to total ductility but not much to the local fracture strain in grains. Also, the number density of microcracks appeared to be lower in the specimen deformed at 700 °C where maximum elongation was obtained, Fig. 12e.

Fig. 13 reveals closer views of microcracks showing their coalescence and propagation. These microcracks are believed to initiate from coarse precipitations or micropores (indicated by arrows) [20] and to preferably propagate following the aggregate boundaries looking clear and thick as indicated in Fig. 2. These observations indicate that the ductility of 14YWT alloy, and possibly the fracture toughness, depends on the local strain level where the microcracking initiates. In general, the fracture behavior of materials produced by powder metallurgy strongly depends on the pore, oxide/carbide distributions, and/or grain shape [21]. A remedy for increasing ductility of such alloy will be more complete degassing.

The re-decrease of ductility with increasing temperature at >700 °C is also confirmed by the enhanced cracking at 800 °C in a side surface view seen in Fig. 14. Observed are many long cracks propagating along the aggregate boundaries. Compared to the cracks shown in Fig. 13, these microcracks are longer and their tips are sharper. It is obvious that these cracks propagate without incurring high local strains at their tips. Similar sharp long cracks were found in the specimen tested at 900 °C and 1000 °C (not shown here). It is believed that the formation of these long cracks

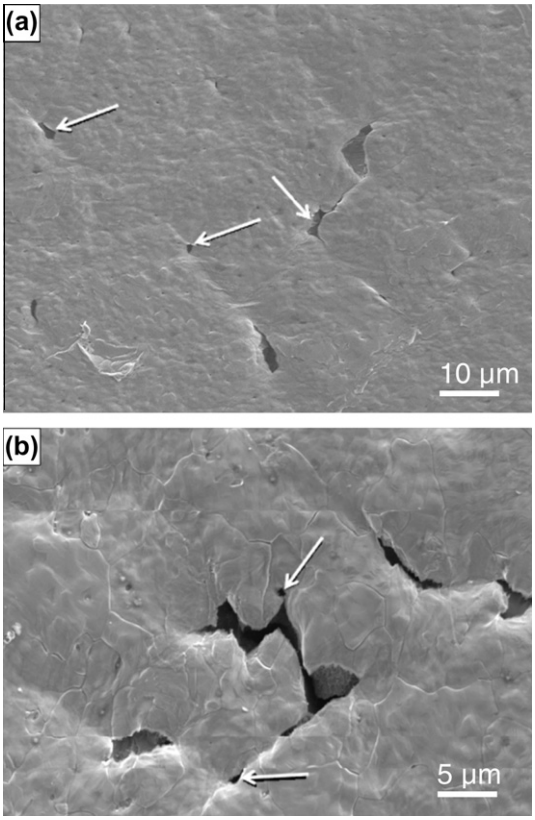

Fig. 13. Details of side surface of specimen broken at (a) 500 °C and (b) 600 °C. Arrows indicate micro-pores.

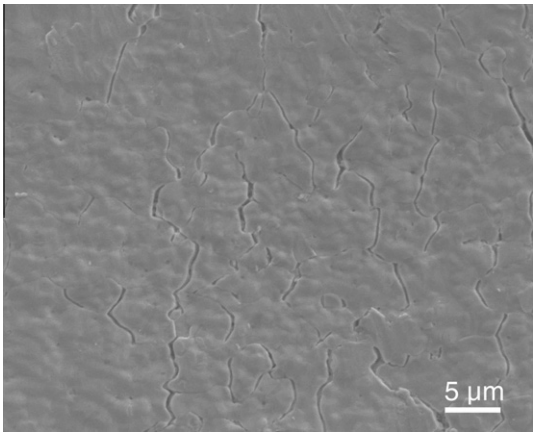

Fig. 14. Side surface of specimen broken at 800 °C.

is related to the strength of aggregate boundaries which become weaker as test temperature increases to or above 800 °C. This low ductility feature is also well in accordance with the discussion about the fracture surface at 900 °C, Fig. 9. A proposed reason for the weakened boundaries at high temperatures > 700 °C is that some solute atoms segregated along the boundaries can be major cause for this boundary decohesion mechanism.

4. Summary and conclusions

High temperature tensile fracture behavior was investigated for the nanoclusters strengthened 14YWT alloy focusing on fracture surface and cracking characteristics. Summary and conclusions are given as follows:

1. The 14YWT SM10 alloy showed much higher strength compared to the comparable alloys such as ODS-EUROFER97 and PM2000. The room temperature YS and UTS of 14YWT SM10 were 1600 MPa and 1749 MPa, respectively.
2. However, poor ductility was measured at most test temperatures: Total elongations were lower than 3% below 500 °C and did not exceed 10% in the high-ductility temperature range of 600–700 °C. The total elongation became lower again to ~3% at higher temperatures ranging from 800 to 1000 °C.
3. Fracture surface examination showed that fracture occurs by a mixed mode fracture consisting of ductile dimple tearing and transgranular cleavage up to 500 °C. At temperatures higher than 600 °C the fracture mode changed to a fully-ductile fracture by dimple formation. At or above 800 °C, the fracture mode became semi-brittle again due to easy boundary separation.
4. Over the entire test temperature range the main cause for poor ductility is believed to be the formation of microcracks initiated at micropores, grain and grain-aggregate boundaries, or coarse precipitates. The so-called aggregate boundaries seem to help crack initiation and propagation. At high temperatures >700 °C, in particular, the weakened aggregate boundaries played a major role in the crack propagation.
5. The present results suggest that the ductility of the 14YWT alloy may be improved by reducing gas-trapped pores and/or by strengthening boundaries via changes in the mechanical alloying and thermo-mechanical treatment conditions.

Acknowledgements

This research was performed at the Oak Ridge National Laboratory, Materials Science and Technology Division and sponsored by the Korea Ministry of Knowledge, Visiting Scientists Program, under IAN: 16B642601, with the US Department of Energy. This research was also sponsored by US Department of Energy, Office of Nuclear Energy under Contract DE-AC05-00OR22725 with UT-Battelle, LLC. The authors would like to express special thanks to Drs. J.T. Busby and L. Tan for their technical reviews and thoughtful comments.

References

[1] L.K. Mansur, in: G.R. Freeman (Ed.), Kinetics of Nonhomogeneous Processes, Springer, New York, NY, 1987 (Chapter 8).
[2] J.J. Huet, V. Leroy, Nucl. Technol. 24 (1974) 216.
[3] S. Ukai, T. Nishida, T. Okuda, T. Yoshitake, J. Nucl. Sci. Technol. 35 (1998) 294–300.
[4] R. Lindau, A. Möslang, M. Schirra, P. Schlossmacher, M. Klimenkov, J. Nucl. Mater. 307–311 (2002) 769.
[5] S. Ukai, M. Fujiwara, J. Nucl. Mater. 307–311 (2002) 749.
[6] S. Ukai, M. Harada, H. Okada, M. Inoue, S. Nomura, S. Shikakura, K. Asabe, T. Nishida, M. Fujiwara, J. Nucl. Mater. 204 (1993) 65.
[7] S. Ukai, M. Harada, H. Okada, M. Inoue, S. Nomura, S. Shikakura, K. Asabe, T. Nishida, M. Fujiwara, J. Nucl. Mater. 204 (1993) 74.
[8] M.K. Miller, D.T. Hoelzer, E.A. Kenik, K.F. Russel, Intermetallics 13 (2005) 387.
[9] D.A. McClintock, M.A. Sokolov, D.T. Hoelzer, R.K. Nanstad, J. Nucl. Mater. 392 (2009) 353–359.
[10] A. Ramar, P. Spätig, R. Schäublin, J. Nucl. Mater. 382 (2008) 210–216.
[11] R. Schäublin, A. Ramar, N. Baluc, V. de Castro, M.A. Monge, T. Leguey, N. Schmid, C. Bonjour, J. Nucl. Mater. 351 (2006) 247–260.
[12] M.A. Sokolov, D.T. Hoelzer, R.E. Stoller, D.A. McClintock, J. Nucl. Mater. 367–370 (2007) 213–216.
[13] D.A. McClintock, D.T. Hoelzer, M.A. Sokolov, R.K. Nanstad, J. Nucl. Mater. 386–388 (2009) 307–311.
[14] D.T. Hoelzer, J. Bentley, M.A. Sokolov, M.K. Miller, G.R. Odette, M.J. Alinger, J. Nucl. Mater. 367–370 (2007) 166–172.
[15] R.L. Klueh, Fusion Eng. Des. 2 (1985) 407–416.
[16] J. Blach, L. Falat, P. Sevc, Eng. Fail. Anal. 16 (2009) 1397–1403.
[17] B. Štefan, A. Vŷrostková, J. Šutorová, J. Fractography'89. In: Proceedings of the 10th Fractographical Conference, Part I. Košice, 1989, p. 170.
[18] K.S. Kumar, S. Suresh, M.F. Chrsholm, J.A. Horton, P. Wang, Acta Mater. 51 (2003) 387.
[19] T.S. Byun, D.T. Hoelzer, G.R. Romanoski, D.A. McClintock, Thermomechanical Behavior of Nanostructured ODS Alloys, ICFRM-14 Conference (2009) Sapporo, Japan.
[20] J.H. Schneibel, C.T. Liu, D.T. Hoelzer, M.J. Mills, P. Sarosi, T. Hayashi, U. Wendt, H. Heyse, Scripta Mater. 57 (2007) 1040–1043.
[21] Z. Oksiuta, N. Baluc, J. Nucl. Mater. 374 (2008) 178–184.